J. Fluid Mech. (1999), *vol.* 382, *pp.* 87–108. Printed in the United Kingdom

Instabilities of dynamic thermocapillary liquid layers with magnetic fields

By T. E. MORTHLAND† AND J. S. WALKER

Department of Mechanical and Industrial Engineering,
University of Illinois, Urbana, IL 61801, USA

(Received 20 August 1997 and in revised form 9 September 1998)

This paper presents a linear-stability analysis for the transition from a steady, two-dimensional thermocapillary convection in a liquid-metal layer to a periodic, three-dimensional flow involving hydrothermal waves which propagate in the direction normal to the plane of the base flow. There is a uniform magnetic field applied parallel to the free surface in the plane of the base flow, and there is a linear temperature gradient along the free surface in the base flow. The ratio of the layer's length to its depth, $2L$, is large. The magnetic Reynolds number is small.

A key parameter is λ, the ratio of the large Hartmann number based on depth to L. The value of λ increases as either the magnetic field strength is increased or L is decreased. The results for very small values of λ agree with the results of a previous treatment of this instability without a magnetic field. As λ is increased, the critical Marangoni number and the wavenumber for the hydrothermal rolls both increase. For large values of λ, the base flow and the hydrothermal waves are confined to a free-surface layer with $O(\lambda^{-1/2})$ dimensionless thickness.

1. Introduction

In the floating-zone process, a liquid bridge of molten semiconductor is held by surface tension between a melting, cylindrical, polycrystalline feed rod and a coaxial, solidifying, cylindrical single crystal. The increase of surface tension from the hottest circumference around the free surface to the colder circumferences at the ends of the crystal and feed rod drives a thermocapillary convection in the melt which is unsteady for virtually all actual processes without a magnetic field. Elements called dopants are added to the melt to give the crystal the desired electrical or optical properties. The unsteady thermocapillary convection produces undesirable spatial oscillations of the dopant concentration in the crystal, called striations. Hurle (1994) reviews floating-zone semiconductor crystal growth.

In his seminal work, Pearson (1958) studied the onset of steady thermocapillary convection in a quiescent fluid layer heated from below. When the heat flux at the bottom of the layer exceeded a critical value, steady cellular convection developed in the layer. In many industrial processes a temperature gradient exists along the free surface which drives fluid from hot to cold regions along the free surface. For this case, a quiescient base state does not exist since any temperature gradient along the free surface produces a thermocapillary convection which is steady as long as the temperature gradient is not too large. Smith & Davis (1983, hereafter referred to as S & D) showed that when the Marangoni number exceeds a critical value, then the

† Present address: 1206 W. Green St., Urbana, IL 61801, USA.

thermocapillary convection involves a new mode of instability called a hydrothermal wave which travels at some oblique angle relative to the steady base flow. The angle of propagation of the hydrothermal wave depends on the Prandtl number. Davis (1987) reviewed advances in the study of thermocapillary instabilities to that date. Velten, Schwabe & Scharmann (1991) investigated the onset of periodic instabilities of thermocapillary convection in a liquid bridge for various Prandtl numbers. In their experiments, they reported seeing hydrothermal waves as predicted by S & D. Riley & Neitzel (1998) recently presented experimental verification of the hydrothermal waves predicted by S & D for low Prandtl number and no magnetic field.

There have been recent advances in the fundamental understanding of thermocapillary instabilities. Shen *et al.* (1990) resolved thermocapillary-driven meridional disturbances in a cylindrical half-zone. In their study, they accurately predict the onset of unsteady thermocapillary convection using energy-stability methods for high Prandtl number fluids. In their direct numerical simulations, Mundrane & Zebib (1992) add the complexity of buoyant convection to the thermocapillary convection in a slot. Experiments performed by Gillon & Homsy (1996) confirm the numerical predictions of Mundrane & Zebib (1993). Laser-Doppler velocimetry experiments performed by Saedeleer *et al.* (1996) indicate the existence of an intermediate flow structure that precedes the development of hydrothermal waves. The structure was reported to be in the form of cells with their axes perpendicular to the temperature gradient which acts along the free surface. Braunsfurth & Homsy (1997) have extended previous experimental studies of combined buoyant–thermocapillary convection in cavities and note a novel oscillatory flow at larger Marangoni numbers. Mercier & Normand (1996) have also investigated combined thermocapillary–buoyancy-driven flows. Recently, Zebib (1996) added the complication of system rotation to thermocapillary instabilities.

For most molten semiconductors, the Prandtl number is less than 0.1, and the electrical conductivity is comparable to that of mercury. If a magnet or solenoid outside the crystal-growth furnace produces a steady magnetic field in the melt, then the electromagnetic (EM) body force can be used to eliminate all unsteadiness in the melt motion and to tailor the residual steady motion in order to optimize the dopant distribution and other crystal properties (Series & Hurle 1991). Robertson & O'Connor (1986) and Croll, Dold & Benz (1994) grew silicon crystals with 0.5 T uniform axial magnetic fields which were parallel to the common centreline of the crystal, floating zone and feed rod. Each crystal had a striation-free central core with greatly reduced striations near the crystal's periphery.

Baumgartl *et al.* (1990) and Rupp *et al.* (1991) presented numerical solutions for the unsteady, three-dimensional thermocapillary convection in a cylindrical floating zone with a uniform axial magnetic field parallel to the free surface. They presented plots of the critical Marangoni number for the transition to unsteady motion versus Hartmann number for the Prandtl numbers of molten silicon and gallium arsenide. Unfortunately, as they acknowledged, they erroneously set the static electric field equal to zero in Ohm's law. As a consequence, Maxwell's equations are not satisfied, electric charge is not conserved, and there is a non-zero normal electric current at the free surface in their numerical solutions. S & D showed that the transition from steady to unsteady thermocapillary convection for low Prandtl number fluids without a magnetic field involves hydrothermal waves which would propagate in a direction nearly orthogonal to the base flow. In the floating-zone geometry, a nearly cylindrical liquid bridge develops, and the free surface is essentially that of a cylinder. For this geometry, temperature gradients along the free surface set up a steady, two-

dimensional base flow in a meridional plane, and the instability is a hydrothermal wave travelling in the azimuthal direction, i.e. one travelling in a direction orthogonal to the base state. In reality, the electrically insulating atmosphere at the free surface blocks the radial electric current which would provide the EM body force opposing the azimuthal velocity at the free surface in the hydrothermal waves. In the numerical solutions of Baumgartl *et al.* (1990) and Rupp *et al.* (1991), there is an erroneous EM body force opposing azimuthal free-surface velocities, so that their results probably overestimate the stabilizing effects of a magnetic field parallel to the free surface.

With large magnetic flux densities, the thermocapillary convection is confined to a very thin boundary layer adjacent to the free surface of the melt. In this boundary layer, curvature effects are negligible (Morthland & Walker 1997), allowing one to use thin fluid layers to model the magnetic damping of thermocapillary convection in floating zones. Wilson (1993) considered the magnetic damping of the onset of steady and unsteady thermocapillary convection in a quiescent layer of an electrically conducting fluid resting on an infinite wall with a uniform vertical temperature gradient and with a uniform magnetic field which was perpendicular to the free surface and wall. In a later study, Wilson (1994) extended his analysis to a non-isothermal wall with heating from below. Both studies included the effects of a deformable free surface. Kaddame & Lebon (1993) also demonstrated the stabilizing effects of a vertical magnetic field on oscillatory instabilities. Wilson showed that if the free surface is allowed to deform, then the stability characteristics of the thermocapillary convection depend on the thermal conditions of the free surface and the influence of gravity waves. In particular, there are always unstable modes present no matter how large the magnetic field is. As an extension to the work of Pearson (1958), Maekawa & Tanasawa (1988) and Wilson (1994), Thess & Nitschke (1995) apply a magnetic field in a direction orthogonal to the plane of the free surface of a fluid layer. They provide physical insight into the structure of the instabilities in magnetically damped thermocapillary flows by applying established principles found in liquid-metal magnetohydrodynamics.

While Wilson considered a magnetic field oriented in a direction perpendicular to the plane of the free surface, a recent study by Priede & Gerbeth (1997) treated the magnetic stabilization of hydrothermal waves with a magnetic field which is parallel to the free surface and which is oriented at an arbitrary angle to the plane of the base flow. In an earlier paper Priede & Gerbeth (1995) treated the effects of a magnetic field which is parallel to the free surface and perpendicular to the plane of the base flow. Both the study by Priede & Gerbeth (1997) and the present study are extensions of the study by S & D which considered an infinite layer without a magnetic field. In the study by Priede & Gerbeth (1997), the fluid layer is still infinite, while the magnetic field strength and its orientation to the base flow are arbitrary. We restrict our study to strong magnetic fields which are parallel to the base flow, and we consider the effect of bounding the layer by endwalls which are perpendicular to the plane of the base flow.

This paper treats the thermocapillary convection in a long layer of a thermally and electrically conducting liquid, as shown in figure 1. There is an electrically and thermally insulating wall at $z^* = 0$, an electrically and thermally insulating inviscid atmosphere at $z^* = d$, electrically insulating isothermal walls with $T^* = \mp bdL$ at $x^* = \pm Ld$, and no boundaries or changes in geometry in the y^*-direction. Here x^*, y^* and z^* are Cartesian coordinates with the unit vectors $\hat{\boldsymbol{e}}_x, \hat{\boldsymbol{e}}_y$ and $\hat{\boldsymbol{e}}_z$, while an asterisk denotes a dimensional variable, and T^* is the deviation of the dimensional temperature from its average value at $x^* = 0$ and $z^* = d$. The deformation of the free

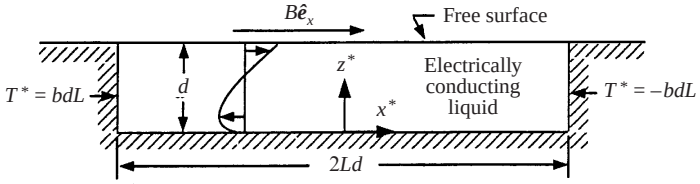

FIGURE 1. Thermocapillary convection in a long liquid layer with a uniform, steady magnetic field $B\hat{e}_x$.

surface involves a balance between the surface tension times the surface curvature and the local pressure or normal stress. Since the characteristic value of the axial pressure gradient here is $(-\mathrm{d}\Gamma/\mathrm{d}T^*)b/d$, the deformation of the free surface is negligible if $\Gamma_0 \gg (-\mathrm{d}\Gamma/\mathrm{d}T^*)bL$, where Γ is the surface tension with a characteristic value Γ_0. This condition also guarantees that the difference between the values of the surface tension at the ends is much smaller than Γ_0. We plan to treat the case of a deformable free surface in a future paper. We also assume that all the liquids properties are uniform except its surface tension Γ at the free surface, which decreases linearly with increasing T^*. There is an externally applied, uniform, steady magnetic field, $B\hat{e}_x$, where B is the magnetic flux density.

Following S & D, we normalize the coordinates with d, the velocity $\boldsymbol{u}^*$ with the characteristic velocity

$$U = \frac{bd}{\mu}\left(-\frac{\mathrm{d}\Gamma}{\mathrm{d}T^*}\right), \tag{1.1}$$

the time t^* with d/U, the pressure p^* with $b(-\mathrm{d}\Gamma/\mathrm{d}T^*)$, and the temperature T^* with bd, where μ is the liquid's absolute viscosity. We also normalize the electric current density $\boldsymbol{j}^*$ with σUB and the electric potential function ϕ^* (voltage) with UBd, where σ is the liquid's electrical conductivity. In addition to the externally applied magnetic field, there is an 'induced' magnetic field produced by the electric currents in the liquid. The characteristic ratio of the induced to applied magnetic fields is the magnetic Reynolds number, $R_m = \mu_p \sigma U d$, where μ_p is the liquid's magnetic permeability. In his classic study of hydrodynamic instabilities with magnetic fields, Chandrasekhar (1961) often assumed that either $R_m \gg 1$ or $R_m = O(1)$ because he was concerned with astrophysical flows. For semiconductor crystal growth from a melt, the value of R_m is always very small, so that we assume that $R_m \ll 1$, and we neglect the induced magnetic field.

The equations governing the dimensionless variables are

$$R\left[\frac{\partial \boldsymbol{u}}{\partial t} + (\boldsymbol{u}\cdot\nabla)\boldsymbol{u}\right] = -\nabla p + Ha^2\,\boldsymbol{j}\times\hat{\boldsymbol{e}}_x + \nabla^2\boldsymbol{u}, \tag{1.2a}$$

$$\nabla\cdot\boldsymbol{u} = 0, \quad \nabla\cdot\boldsymbol{j} = 0, \tag{1.2b,c}$$

$$\boldsymbol{j} = -\nabla\phi + \boldsymbol{u}\times\hat{\boldsymbol{e}}_x, \tag{1.2d}$$

$$M\left[\frac{\partial T}{\partial t} + \boldsymbol{u}\cdot\nabla T\right] = \nabla^2 T, \tag{1.2e}$$

where

$$R = \frac{\rho U d}{\mu}, \quad Ha = Bd\left(\frac{\sigma}{\mu}\right)^{1/2}, \quad M = Pr\,R, \quad Pr = \frac{\mu c_p}{\kappa} \tag{1.3a–d}$$

are the Reynolds, Hartmann, Marangoni and Prandtl numbers, respectively, while ρ, c_p and κ are the liquid's density, specific heat and thermal conductivity. The Navier–Stokes equation (1.2*a*) includes the electromagnetic (EM) body force due to $\boldsymbol{j}$ and the dimensionless magnetic field $\hat{\boldsymbol{e}}_x$. The solubility condition (1.2*c*) guarantees the existence of a solution of Maxwell's equations for the $O(R_m)$ induced magnetic field which is ignored here. Ohm's law (1.2*d*) includes the static electric field $-\nabla\phi$ due to electric charges and the induced electric field due to the motion across magnetic field lines. Joule heating and viscous dissipation are neglected in the conservation of internal energy (1.2*e*) because both are negligible compared to the heat transfer from the heater through the melt to the crystal in any crystal-growth process (Langlois & Lee 1983). The boundary conditions are

$$\boldsymbol{u} = 0, \quad j_z = 0, \quad \frac{\partial T}{\partial z} = 0, \quad \text{at} \quad z = 0, \tag{1.4a–c}$$

$$\frac{\partial u}{\partial z} = -\frac{\partial T}{\partial x}, \quad \frac{\partial v}{\partial z} = -\frac{\partial T}{\partial y}, \quad w = 0, j_z = 0, \quad \frac{\partial T}{\partial z} = 0, \quad \text{at} \quad z = 1, \tag{1.5a–e}$$

$$\boldsymbol{u} = 0, \quad j_x = 0, \quad T = \mp L, \quad \text{at} \quad x = \pm L, \tag{1.6a–c}$$

where $\boldsymbol{u} = u\hat{\boldsymbol{e}}_x + v\hat{\boldsymbol{e}}_y + w\hat{\boldsymbol{e}}_z$. In the floating-zone (FZ) process, the melt forms a roughly cylindrical liquid bridge between a melting feed rod and a solidifying crystal. The liquid–solid interfaces are isothermal, while the electrical conductivity of the solid semiconductor is typically one-twentieth that of the liquid. These interfaces correspond qualitatively to the electrically insulating, isothermal walls at $x = \pm L$.

S & D presented a linear stability analysis for an infinitely long liquid layer ($L = \infty$) without a magnetic field ($Ha = 0$). For $Ha = 0$, end effects are negligible and the infinite-layer solutions apply as long as $L \gg 1$ (Sen & Davis 1982). From S & D,

$$\boldsymbol{u} = \left(\tfrac{3}{4}z^2 - \tfrac{1}{2}z\right)\hat{\boldsymbol{e}}_x + \epsilon\boldsymbol{u}'(z)\exp[\mathrm{i}(k_x x + k_y y - \alpha t)], \tag{1.7a}$$

$$T = -x + \frac{M}{48}(4z^3 - 3z^4 - 1) + \epsilon T'(z)\exp[\mathrm{i}(k_x x + k_y y - \alpha t)], \tag{1.7b}$$

where $O(\epsilon^2)$ terms are neglected, $\boldsymbol{u}'$ and T' are complex modal functions, k_x and k_y are real wavenumbers, $\alpha = \alpha_r + \mathrm{i}\alpha_i$, α_r is the circular frequency, and α_i is the attenuation ($\alpha_i < 0$) or amplification ($\alpha_i > 0$) factor. S & D found that the instability involves plane 'hydrothermal' waves propagating at angles of $\pm\theta$ to the (x, z)-plane, where $\theta = \arctan(k_y/k_x)$. These hydrothermal waves involve rolls with a phase shift between the perturbation velocity and temperature. A hot line along the free surface drives a flow which brings cold liquid to this line, but inertia causes the flow to continue after convective heat transfer has eliminated the local free-surface temperature elevation. The continuing flow creates a cold line which first stops the flow and then creates a reverse flow that brings hot fluid to this line. This process continues, thereby establishing the oscillatory motion (Smith 1986).

As M is increased from zero for a fixed value of Pr, one must search over all possible pairs of values of k_x and k_y in order to find that for which the first non-negative value of α_i occurs. For this critical mode, S & D found that the critical Marangoni number M_c, the propagation angle θ, the dimensionless period $2\pi/\alpha_r$ and the dimensionless wavelength $2\pi(k_x^2 + k_y^2)^{-1/2}$ depend on the value of Pr. Since $Pr < 0.1$ for virtually all molten semiconductors, we only discuss the results in figures 17 and 18 of S & D for this range. For $Pr < 0.1$, $\theta > 75°$, and the M_c for the correct critical combination of k_x and k_y is only slightly less than the critical Marangoni

number M_{c0} for $k_x = 0$, i.e. for hydrothermal waves propagating in the y-direction with all perturbation variables independent of x. The value of $(M_{c0} - M_c)$ is small for $Pr = 0.1$ and decreases rapidly as Pr is decreased.

As long as $L = \infty$, the addition of a magnetic field $B\hat{\boldsymbol{e}}_x$ provides EM damping of a perturbation with $k_x \neq 0$, but has no effect on a perturbation with $k_x = 0$ (Chandrasekhar 1961). The curl of (1.2*d*) with (1.2*b*) gives

$$\nabla \times \boldsymbol{j} = \frac{\partial \boldsymbol{u}}{\partial x}. \tag{1.8}$$

If $\boldsymbol{u}$ is independent of x, then the solution of (1.2*c*) and (1.8) is $\boldsymbol{j} = 0$, so that $\nabla\phi = \boldsymbol{u} \times \hat{\boldsymbol{e}}_x$. As long as the velocity does not vary along magnetic field lines, a static electric field develops which exactly cancels the induced electric field, so that there are no electric currents and no EM body forces. Priede & Gerbeth (1997) recently presented a linear stability analysis for this problem with $L = \infty$ and with an arbitrary value of Ha. Their results for $Pr = 0.01$ and $Pr = 0.03$ show that, as Ha is increased, k_x goes to zero, θ increases to 90°, and M_c increases to M_{c0}. Once k_x reaches zero at approximately $Ha = 500$, further increases in Ha have no effect on the instability. Here we assume that $Ha \gg 1$, so that $k_x = 0$ for the critical mode for $L = \infty$, and all variables have the appropriate symmetry about the $x = 0$ plane for $L = O(Ha)$. Priede & Gerbeth (1997) also consider magnetic fields at an angle α_B to the (x, z)-plane. They showed that, as Ha is increased, θ approaches $(\alpha_B + 90°)$, i.e. the vorticity in the plane hydrothermal waves becomes aligned with the magnetic field. We only consider magnetic fields which are parallel to the (x, z)-plane, since this corresponds to the FZ process with an axial magnetic field.

The effects of the magnetic field become significant when L is finite. As $\boldsymbol{u}$ decreases to zero at $x = \pm L$, the local difference between $\nabla\phi$ and $\boldsymbol{u} \times \hat{\boldsymbol{e}}_x$ drives electric currents whose circuits and EM body forces may extend far from the ends. If a hydrothermal wave for $L = \infty$ and $k_x = 0$ is a generator on open-circuit, then the boundary layers at $x = \pm L$ provide paths for leakage currents. If the magnetic field is strong ($Ha \gg 1$), then even remote ends for $L \gg 1$ can lead to leakage currents with $O(1)$ EM damping. Here we present asymptotic solutions for $L \gg 1$ and $Ha \gg 1$ with the constraint that $\lambda = Ha/L$ is an $O(1)$ parameter. The solutions for small values of λ should correspond to the solutions of S & D for $k_x = 0$, since a magnetic field with $Ha \geqslant 500$ will align the hydrothermal waves for $L = \infty$ (Priede & Gerbeth 1997). We can achieve a smooth transition from the S & D solutions for $k_x = 0$ either by fixing a large value of L and increasing the magnetic field strength or by applying a fixed, strong magnetic field and decreasing L from infinity.

2. Base flow

For the normal mode analysis in (1.7) with $k_x = 0$, the eigenvalues occur in pairs, $(\pm\alpha_r + \mathrm{i}\alpha_i)$, corresponding to a pair of identical hydrothermal waves, propagating with the same phase velocity (α_r/k_y) in the $\pm y$-directions. For each pair of modes, there is an infinite number of solutions corresponding to an arbitrary ratio of the amplitudes in the superposition of the two waves propagating in opposite directions. With no loss of generality, we can make the solution unique for each pair of modes by considering the superposition with equal amplitudes, leading to a standing wave. While the standing wave does not propagate, it has the same circular frequency α_r for each wavenumber k_y as the pair of propagating waves, while the non-moving

wave pattern is identical to the moving wave pattern in either propagating wave. The equivalence of the standing wave to the propagating waves is also true for finite values of L, as long as the perturbation variables have the appropriate symmetries about $x = 0$, and the critical modes always have these symmetries for $Ha \geqslant 500$ and $Pr \leqslant 0.1$ (Priede & Gerbeth 1997). For u, w, p and j_y, we introduce the form

$$u = \bar{u}(x, z) + \epsilon u'(x, z, t)\cos(k_y y), \tag{2.1a}$$

while

$$T = -x + \bar{T}(x, z) + \epsilon T'(x, z, t)\cos(k_y y); \tag{2.1b}$$

for v, ϕ, j_x and j_z, we introduce the form

$$v = \epsilon v'(x, z, t)\sin(k_y y). \tag{2.1c}$$

The overbars and primes denote the base-flow and linear-perturbation variables, respectively. The form (2.1) does not exclude oblique waves. For an infinite length, the direction of the critical plane wave is determined by searching over all combinations of k_x and k_y in (1.7). For a finite length, all possible x variations are included in the modal functions such as $u'(x, z, t)$ in (2.1). If the critical mode for a finite length involves the equivalent of an oblique wave with $k_x \neq 0$ for an infinite length, then the modal functions in (2.1) would not be even functions of x. If the modal functions in (2.1) are all symmetric about the $x = 0$ plane, then the critical mode involves the finite-length equivalent of a plane wave propagating at right angles to the plane of the base flow, but the structure of this wave is three-dimensional since end effects extend over the entire fluid layer for $L = O(Ha)$. For the base flow, (1.2) and (1.4)–(1.6) become

$$R\left[\bar{u}\frac{\partial \bar{u}}{\partial x} + \bar{w}\frac{\partial \bar{u}}{\partial z}\right] = -\frac{\partial \bar{p}}{\partial x} + \frac{\partial^2 \bar{u}}{\partial x^2} + \frac{\partial^2 \bar{u}}{\partial z^2}, \tag{2.2a}$$

$$R\left[\bar{u}\frac{\partial \bar{w}}{\partial x} + \bar{w}\frac{\partial \bar{w}}{\partial z}\right] = -\frac{\partial \bar{p}}{\partial z} - Ha^2 \bar{j}_y + \frac{\partial^2 \bar{w}}{\partial x^2} + \frac{\partial^2 \bar{w}}{\partial z^2}, \tag{2.2b}$$

$$\frac{\partial \bar{u}}{\partial x} + \frac{\partial \bar{w}}{\partial z} = 0, \quad \bar{j}_y = \bar{w}, \tag{2.2c,d}$$

$$M\left[\bar{u}\left(-1 + \frac{\partial \bar{T}}{\partial x}\right) + \bar{w}\frac{\partial \bar{T}}{\partial z}\right] = \frac{\partial^2 \bar{T}}{\partial x^2} + \frac{\partial^2 \bar{T}}{\partial z^2}, \tag{2.2e}$$

$$\bar{u} = 0, \quad \bar{w} = 0, \quad \frac{\partial \bar{T}}{\partial z} = 0, \quad \text{at} \quad z = 0, \tag{2.3a–c}$$

$$\frac{\partial \bar{u}}{\partial z} = 1 - \frac{\partial \bar{T}}{\partial x}, \quad \bar{w} = 0, \quad \frac{\partial \bar{T}}{\partial z} = 0, \quad \text{at} \quad z = 1, \tag{2.3d–f}$$

$$\bar{u} = 0, \quad \bar{w} = 0, \quad \bar{T} = 0, \quad \text{at} \quad x = \pm L. \tag{2.3g–i}$$

For $Ha \gg 1$ and $L = Ha/\lambda$, where λ is an $O(1)$ parameter, the liquid region can be divided into: (i) a central core region where $\partial/\partial x = O(Ha^{-1})$, and (ii) Hartmann layers with an $O(Ha^{-1})$ thickness adjacent to the ends at $x = \pm L$. For the core we introduce the scale compression $X = x/L = \lambda x/Ha$ and the asymptotic expansions

$$\bar{u} = u_c(X, z) + O(Ha^{-1}), \quad \bar{w} = Ha^{-1} w_c(X, z) + O(Ha^{-2}), \tag{2.4a,b}$$

$$\bar{p} = Ha\, p_c(X, z) + O(1), \quad \bar{T} = T_c(X, z) + O(Ha^{-1}). \tag{2.4c,d}$$

For the core, the leading-order terms in (2.2) are

$$0 = -\lambda \frac{\partial p_c}{\partial X} + \frac{\partial^2 u_c}{\partial z^2}, \quad 0 = -\frac{\partial p_c}{\partial z} - w_c, \tag{2.5a,b}$$

$$\lambda \frac{\partial u_c}{\partial X} + \frac{\partial w_c}{\partial z} = 0, \quad -Mu_c = \frac{\partial^2 T_c}{\partial z^2}. \tag{2.5c,d}$$

We introduce a stream function $\psi_c(X, z)$ and another integration function $F_c(X, z)$ in order to satisfy (2.5*c*) and (2.5*b*), respectively,

$$u_c = \frac{\partial \psi_c}{\partial z}, \quad w_c = -\lambda \frac{\partial \psi_c}{\partial X}, \tag{2.6a,b}$$

$$\psi_c = \frac{\partial F_c}{\partial z}, \quad p_c = \lambda \frac{\partial F_c}{\partial X}. \tag{2.6c,d}$$

Equations (2.5*a*), (2.5*d*) and (2.3*a–f*) become

$$\frac{\partial^4 F_c}{\partial z^4} = \lambda^2 \frac{\partial^2 F_c}{\partial X^2}, \quad \frac{\partial^2 T_c}{\partial z^2} = -M \frac{\partial^2 F_c}{\partial z^2}, \tag{2.7a,b}$$

$$\frac{\partial F_c}{\partial z} = 0, \quad \frac{\partial^2 F_c}{\partial z^2} = 0, \quad \frac{\partial T_c}{\partial z} = 0, \quad \text{at} \quad z = 0, \tag{2.8a–c}$$

$$\frac{\partial F_c}{\partial z} = 0, \quad \frac{\partial^3 F_c}{\partial z^3} = 1, \quad \frac{\partial T_c}{\partial z} = 0, \quad \text{at} \quad z = 1. \tag{2.8d–f}$$

The Hartmann layers match any values of the $O(Ha^{-1})$ $\bar{w}$ in the core, while the jumps in $\bar{u}$ and $\bar{T}$ across the Hartmann layers are $O(Ha^{-2})$ and $O(Ha^{-4})$, respectively (Walker, Ludford & Hunt 1972). Therefore the appropriate boundary conditions on the core variables are

$$u_c = 0, \quad T_c = 0, \quad \text{at} \quad X = \pm 1. \tag{2.9a,b}$$

Eliminating arbitrary additive constants in p_c and F_c, (2.9*a*) becomes

$$F_c = 0, \quad \text{at} \quad X = \pm 1. \tag{2.10}$$

The separation-of-variables solution for F_c is

$$\begin{aligned} F_c = \sum_{n=0}^{\infty} A_n \cos\left[\left(n + \tfrac{1}{2}\right)\pi X\right] \{&[\sinh(\gamma_n)\cos(\gamma_n) - \cosh(\gamma_n)\sin(\gamma_n)] \\ &\times [\cosh(\gamma_n z)\sin(\gamma_n z) - \sinh(\gamma_n z)\cos(\gamma_n z)] \\ &-2\sinh(\gamma_n)\sin(\gamma_n)\cosh(\gamma_n z)\cos(\gamma_n z)\}, \end{aligned} \tag{2.11a}$$

$$A_n = (-1)^n \pi^{-1} \left(n + \tfrac{1}{2}\right)^{-1} \gamma_n^{-3} \left[\sinh(2\gamma_n) - \sin(2\gamma_n)\right]^{-1}, \tag{2.11b}$$

$$\gamma_n = \tfrac{1}{2}\left[\lambda\pi(2n+1)\right]^{1/2}. \tag{2.11c}$$

This solution for the base flow in the core parallels the separation-of-variables solutions for magnetohydrodynamic flows in rectangular ducts, which were presented by Hunt (1965). The advantage of this solution is the exponential behaviour in z, which leads to improved convergence of the series as the value of λ is increased. For $\lambda \gg 1$, the present core is split into a stagnant region and a free-surface layer with an $O(\lambda^{-1/2})$ thickness. The solution (2.11) automatically becomes the solution for the free-surface layer, when we introduce $\zeta = \lambda^{1/2}(z - 1)$, let $\lambda \to \infty$ and neglect terms with $\exp(-2\gamma_n)$. Because of the exponential behaviour in z and the behaviour with λ, a few hundred terms or less in the truncated series were required for acceptable convergence.

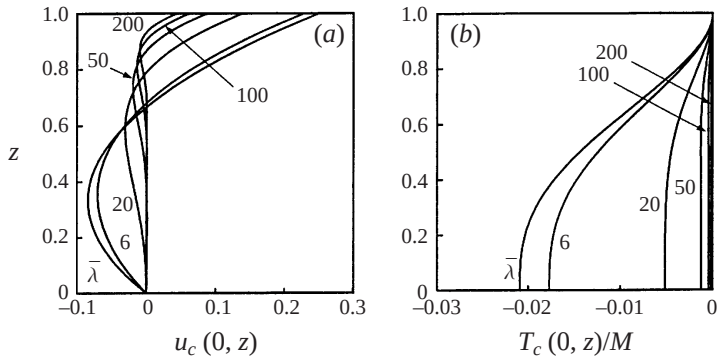

FIGURE 2. Base-flow axial velocity u_c and temperature T_c/M versus z at $X = 0$ (i) for $\lambda \leqslant \bar{\lambda}$, which are identical to the results of S & D, where $\bar{\lambda} = 2$ and (ii) $\lambda = 6, 20, 50, 100$ and 200. (*a*) $u_c(0, z)$, (*b*) $T_c(0, z)/M$.

With (2.7*b*), (2.8*a*) and (2.8*d*), (2.8*c*) and (2.8*f*) are redundant. Following S & D, we add a very small heat transfer coefficient between the free surface and a parallel surface with dimensionless temperature $T = -x$. Then integrating (2.7*b*) twice and with these boundary conditions gives

$$T_c(X, z) = M\,[F_c(X, 1) - F_c(X, z)]\,. \tag{2.12}$$

Plots of the base-flow axial velocity u_c and temperature T_c at $X = 0$ for six values of λ are presented in figure 2. For $\lambda \leqslant \bar{\lambda}$, where $\bar{\lambda} = 2$, $u_c(0, z)$ and $T_c(0, z)$ are essentially identical to the base-flow values of S & D, which are given by the polynomials in (1.7). The curves for $\lambda \leqslant \bar{\lambda}$ coincide with the S & D curves in figure 2. The circuit for the axial flows in the $\pm x$-directions must be completed by vertical flows near the ends at $x = \pm L$. There is no EM body force opposing u_c, but there is a strong EM body force opposing w_c. As long as $L \geqslant Ha/2$, the opposition to vertical flows near $x = \pm L$ is too weak to prevent the spread of the flow over the entire depth and the realization of the S & D profiles for $L = \infty$ near $x = 0$. Priede & Gerbeth (1997) reached the same conclusion. As L is decreased from $Ha/2$, the EM body force opposing w_c becomes a major addition to the viscous opposition to the flow, as assumed in (1.1), and prevents the spread of the flow away from the free surface. For $L = O(1)$, the thermocapillary convection is confined to a free-surface layer with an $O(Ha^{-1/2})$ thickness, and there is no flow in the region below this layer to all orders in Ha (Morthland & Walker 1997). The free-surface layer is illustrated by the streamlines for $\lambda = 200$ and $X \geqslant 0$, which are plotted in figure 3(*b*), and is contrasted with the streamlines for $\lambda = 1$ (figure 3*a*). With the flow confined to a thin layer and with the same driving force at the free surface, the velocities decrease as λ is increased, and the values of T_c due to convection of the base temperature $\bar{T} = -x$ also decrease. As soon as $\partial u_c/\partial z$ is essentially zero at $z = 0$, the bottom wall ceases to play any role, and we expect the solution to correspond to a free-surface layer with an $O(\lambda^{-1/2})$ thickness. Indeed, for $\lambda \geqslant 20$, the maximum free-surface velocity $u_c(0, 1) = 0.62\lambda^{-1/2}$, the minimum value of the stream function $\psi_{c\,min} = -0.24\lambda^{-1}$, and the temperature change outside the free-surface layer $T_c(0, 0) = -0.43\lambda^{-3/2}$. We have computed these scalings from the numerical results. For the case of large λ, there exists a well-defined boundary-layer flow of $O(\lambda^{-1/2})$ thickness adjacent to the free surface (Morthland & Walker 1997). In a future paper, we plan to treat the stability of this boundary-layer flow.

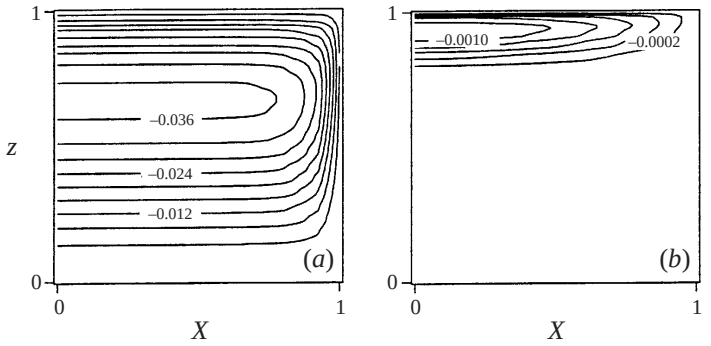

FIGURE 3. Streamlines for the core base flow for (*a*) $\lambda = 1$ and (*b*) $\lambda = 200$. Hartmann layers match the non-zero values of w_c at $X = \pm 1$.

3. Instabilities

We introduce (2.1) into (1.2) and neglect $O(\epsilon^2)$ terms,

$$R\left[\frac{\partial u'}{\partial t} + \bar{u}\frac{\partial u'}{\partial x} + \frac{\partial \bar{u}}{\partial x}u' + \bar{w}\frac{\partial u'}{\partial z} + \frac{\partial \bar{u}}{\partial z}w'\right] = -\frac{\partial p'}{\partial x} + \nabla^2 u', \tag{3.1a}$$

$$R\left[\frac{\partial v'}{\partial t} + \bar{u}\frac{\partial v'}{\partial x} + \bar{w}\frac{\partial v'}{\partial z}\right] = k_y p' + Ha^2 j_z' + \nabla^2 v', \tag{3.1b}$$

$$R\left[\frac{\partial w'}{\partial t} + \bar{u}\frac{\partial w'}{\partial x} + \frac{\partial \bar{w}}{\partial x}u' + \bar{w}\frac{\partial w'}{\partial z} + \frac{\partial \bar{w}}{\partial z}w'\right] = -\frac{\partial p'}{\partial z} - Ha^2 j_y' + \nabla^2 w', \tag{3.1c}$$

$$\frac{\partial u'}{\partial x} + k_y v' + \frac{\partial w'}{\partial z} = 0, \quad \frac{\partial j_x'}{\partial x} - k_y j_y' + \frac{\partial j_z'}{\partial z} = 0, \tag{3.1d,e}$$

$$j_x' = -\frac{\partial \phi'}{\partial x}, \quad j_y' = -k_y\phi' + w', \quad j_z' = -\frac{\partial \phi'}{\partial z} - v', \tag{3.1f–h}$$

$$M\left[\frac{\partial T'}{\partial t} + \bar{u}\frac{\partial T'}{\partial x} + \left(-1 + \frac{\partial \bar{T}}{\partial x}\right)u' + \bar{w}\frac{\partial T'}{\partial z} + \frac{\partial \bar{T}}{\partial z}w'\right] = \nabla^2 T'. \tag{3.1i}$$

where now

$$\nabla^2 = \frac{\partial^2}{\partial x^2} + \frac{\partial^2}{\partial z^2} - k_y^2. \tag{3.1j}$$

If the leading-order terms in the asymptotic expansions of (3.1*d*) and (3.1*e*) are used, this leads to a redundant set of equations. Consequently, two terms in the asymptotic expansions of (3.1*d*) and (3.1*e*) are needed in order to satisfy uniqueness. We can avoid sorting orders if we replace these equations with two equivalent ones. Equation (3.1*e*) is replaced by an axial vorticity equation. Combining (3.1*e*), (3.1*f*), (3.1*g*) and (3.1*h*), we find that the axial vorticity is related to the electric potential function,

$$\frac{\partial v'}{\partial z} + k_y w' = -\nabla^2 \phi'. \tag{3.2}$$

In the discussion of (1.8), we noted that a vortex aligned with a magnetic field produces a voltage distribution so that $\nabla\phi$ cancels or nearly cancels $\boldsymbol{u} \times \hat{\boldsymbol{e}}_x$, e.g. low voltage at the centre of a vortex and high voltage at its periphery produce a radial electric field to balance $\boldsymbol{u} \times \hat{\boldsymbol{e}}_x$. We solve (3.1*b*) and (3.1*c*) for j_z' and j_y', respectively, we introduce these expressions and (3.1*f*) into (3.1*e*), and we use (3.2) for the axial

vorticity in order to obtain the equation to replace (3.1*e*),

$$R\left[\frac{\partial}{\partial t}\nabla^2\phi' + \bar{u}\frac{\partial}{\partial x}\nabla^2\phi' + \bar{w}\frac{\partial}{\partial z}\nabla^2\phi' + \frac{\partial \bar{w}}{\partial z}\nabla^2\phi' - k_y\frac{\partial \bar{w}}{\partial x}u' - \frac{\partial \bar{u}}{\partial z}\frac{\partial v'}{\partial x}\right] = -Ha^2\frac{\partial^2\phi'}{\partial x^2} + \nabla^4\phi'. \quad (3.3)$$

The EM damping of vorticity aligned with the magnetic field arises because the vorticity goes to zero across each Hartmann layer, so that the locally unbalanced voltage variation drives electric currents inside each Hartmann layer. The circuit for these Hartmann-layer currents must be completed through the core, producing the EM damping in the core. With symmetric axial vorticity, the values of $j_x = -\partial\phi/\partial x$ between the Hartmann layers and core have opposite signs at $x = \pm L$. The $\partial^2\phi'/\partial x^2$ in (3.3) represents the fringing of the Hartmann-layer currents through the core and the associated EM damping of the axial vorticity.

It turns out that the axial velocity gradient $\partial u'/\partial x$ is much smaller than the other two terms in (3.1*d*), but it is still very important. Therefore we derive an axial velocity gradient equation to replace (3.1*d*). We introduce our expressions for j_z' and j_y' from (3.1*b*) and (3.1*c*) into (3.1*h*) and (3.1*g*), respectively, and we introduce the resultant expressions for v' and w' into (3.1),

$$R\left[\frac{\partial^2 u'}{\partial x\partial t} + \bar{u}\frac{\partial^2 u'}{\partial x^2} + \bar{w}\frac{\partial^2 u'}{\partial x\partial z} - \frac{\partial \bar{u}}{\partial z}\frac{\partial w'}{\partial x} - \frac{\partial^2 \bar{w}}{\partial x\partial z}u' - \frac{\partial \bar{w}}{\partial x}\frac{\partial u'}{\partial z} - 2\frac{\partial \bar{w}}{\partial z}\frac{\partial w'}{\partial z} - \frac{\partial^2 \bar{w}}{\partial z^2}w'\right] = -Ha^2\frac{\partial u'}{\partial x} + \left(\frac{\partial^2 p'}{\partial z^2} - k_y^2 p'\right) + \nabla^2\left(\frac{\partial u'}{\partial x}\right). \quad (3.4)$$

The boundary conditions are

$$u' = 0, \quad v' = 0, \quad w' = 0, \quad j_z' = 0, \quad \frac{\partial T'}{\partial z} = 0, \quad \text{at} \quad z = 0, \qquad (3.5a\text{–}e)$$

$$\frac{\partial u'}{\partial z} = -\frac{\partial T'}{\partial x}, \quad \frac{\partial v'}{\partial z} = k_y T', \quad w' = 0, \quad j_z' = 0, \quad \frac{\partial T'}{\partial z} = 0, \quad \text{at} \quad z = 1, \quad (3.6a\text{–}e)$$

$$u' = 0, \quad v' = 0, \quad w' = 0, \quad j_x' = 0, \quad T' = 0, \quad \text{at} \quad x = \pm L. \qquad (3.7a\text{–}e)$$

For the core, we introduce the same axial-scale compression and the same base-flow asymptotic expansions (2.4). We choose ϵ as the characteristic magnitude of the perturbation velocity in the core, so that the asymptotic expansions for u', v', w', ϕ', and T' in the core have the form

$$u' = u_1(X, z, t) + O(Ha^{-1}), \qquad (3.8a)$$

and those for j_x', j_y' and j_z' have the form

$$j_x' = Ha^{-1} j_{x1}(X, z, t) + O(Ha^{-2}), \qquad (3.8b)$$

while

$$p' = Ha\, p_1(X, z, t) + O(1). \qquad (3.8c)$$

The leading-order terms in the linearized Navier–Stokes equations (3.1*a–c*) are

$$R\left[\frac{\partial u_1}{\partial t} + \frac{\partial u_c}{\partial z}w_1\right] = -\lambda\frac{\partial p_1}{\partial X} + \nabla^2 u_1, \qquad (3.9a)$$

$$j_{z1} = -k_y p_1, \quad j_{y1} = -\frac{\partial p_1}{\partial z}, \qquad (3.9b,c)$$

where now

$$\nabla^2 = \frac{\partial^2}{\partial z^2} - k_y^2. \tag{3.9d}$$

The leading-order terms in Ohm's law (3.1*f–h*) and the linearized internal-energy equation (3.1*i*) are

$$j_{x1} = -\lambda \frac{\partial \phi_1}{\partial X}, \quad w_1 = k_y \phi_1, \quad v_1 = -\frac{\partial \phi_1}{\partial z} \tag{3.10a–c}$$

$$M\left[\frac{\partial T_1}{\partial t} - u_1 + \frac{\partial T_c}{\partial z} w_1\right] = \nabla^2 T_1. \tag{3.10d}$$

The expressions (3.10*b*) and (3.10*c*) from Ohm's law automatically satisfy the $O(1)$ terms in (3.1*d*) without providing an equation for the $O(Ha^{-1})$ $\partial u'/\partial x$. Similarly the expressions (3.9*b*) and (3.9*c*) from the Navier–Stokes equations automatically satisfy the $O(Ha^{-1})$ terms in (3.1*e*) without providing an equation for the $O(Ha^{-2})$ $\partial j_x'/\partial x = -\partial^2 \phi'/\partial x^2$. The leading-order terms in (3.3) and (3.4) are

$$R\frac{\partial}{\partial t}\nabla^2 \phi_1 = -\lambda^2 \frac{\partial^2 \phi_1}{\partial X^2} + \nabla^4 \phi_1, \tag{3.11a}$$

$$\lambda \frac{\partial u_1}{\partial X} = \nabla^2 p_1. \tag{3.11b}$$

We introduce an integration function $F_1(X, z, t)$ in order to satisfy (3.11*b*),

$$u_1 = \nabla^2 F_1, \quad p_1 = \lambda \frac{\partial F_1}{\partial X}. \tag{3.12a,b}$$

Introducing (3.10*b*) and (3.12), (3.9*a*) and (3.10*d*) become

$$R\frac{\partial}{\partial t}\nabla^2 F_1 = -\lambda^2 \frac{\partial^2 F_1}{\partial X^2} + \nabla^4 F_1 - R k_y \frac{\partial u_c}{\partial z}\phi_1, \tag{3.13a}$$

$$\frac{\partial T_1}{\partial t} = M^{-1}\nabla^2 T_1 + \nabla^2 F_1 - k_y \frac{\partial T_c}{\partial z}\phi_1. \tag{3.13b}$$

Equations (3.11*a*) and (3.13) govern ϕ_1, F_1 and T_1, while the other core perturbation variables are given by (3.9*b*), (3.9*c*), (3.10*a*), (3.10*b*), (3.10*c*), and (3.12). The boundary conditions (3.5) and (3.6) become

$$\phi_1 = 0, \quad \frac{\partial \phi_1}{\partial z} = 0, \quad F_1 = 0, \quad \frac{\partial^2 F_1}{\partial z^2} = 0, \quad \frac{\partial T_1}{\partial z} = 0, \quad \text{at} \quad z = 0. \tag{3.14a–e}$$

$$\phi_1 = 0, \quad \frac{\partial^2 \phi_1}{\partial z^2} + k_y T_1 = 0, \quad F_1 = 0, \tag{3.15a–c}$$

$$\frac{\partial^3 F_1}{\partial z^3} - k_y^2 \frac{\partial F_1}{\partial z} = 0, \quad \frac{\partial T_1}{\partial z} = 0, \quad \text{at} \quad z = 1. \tag{3.15d,e}$$

Since u_1 and p_1 are uniquely defined, the F_1 defined by (3.12) has an arbitrary additive function

$$f_1(t)\exp(k_y z) + f_2(t)\exp(-k_y z), \tag{3.16}$$

for any functions f_1 and f_2 of time. The boundary conditions (3.5*d*) and (3.6*d*) with (3.9*b*) and (3.12*b*) imply that F_1 equals an arbitrary function of time at $z = 0$ or at $z = 1$. By setting these two functions of time equal to zero in (3.14*c*) and (3.15*c*), we eliminate the homogeneous solution (3.16) and make F_1 unique.

The Hartmann layers at $x = \pm L$ match any values of the tangential core velocities

v and w, provided the core solution satisfies the Hartmann conditions (Walker *et al.* 1972),

$$u = \mp Ha^{-1}\left[\frac{\partial v}{\partial y} + \frac{\partial w}{\partial z}\right], \tag{3.17a}$$

$$j_x = \pm Ha^{-1}\left[\frac{\partial v}{\partial z} - \frac{\partial w}{\partial y}\right] \quad \text{at} \quad x = \pm L, \tag{3.17b}$$

where (3.17*b*) shows that the axial electric current density between a Hartmann layer and the core is proportional to the axial core vorticity. The leading-order terms in (3.17) for the core perturbation are

$$u_1 = 0, \quad j_{x1} = \pm\left[\frac{\partial v_1}{\partial z} + k_y w_1\right], \quad \text{at} \quad X = \pm 1. \tag{3.18a,b}$$

With (3.10*a*), (3.10*b*), (3.10*c*), and (3.12*a*), and with continuity of F_1 at $X = \pm 1$ and $z = 0$ or $z = 1$, (3.18) become

$$F_1 = 0, \quad \lambda\frac{\partial \phi_1}{\partial X} = \pm\nabla^2\phi_1, \quad \text{at} \quad X = \pm 1. \tag{3.19a,b}$$

Since the jump in T_1 is $O(Ha^{-4})$ across the Hartmann layers,

$$T_1 = 0 \quad \text{at} \quad X = \pm 1. \tag{3.19c}$$

4. Numerical solution

The linear, transient and variable-coefficient partial differential equations that govern the unknowns ϕ_1, F_1, and T_1 for $-1 \leqslant X \leqslant 1$, $0 \leqslant z \leqslant 1$ and $t \geqslant 0$ are given by (3.11*a*), (3.13*a*), and (3.13*b*). These equations are subject to the boundary conditions given by (3.14), (3.15), and (3.19). Since this boundary value problem is homogeneous, we compute initial conditions for the perturbation variables. First we replace (3.15*e*) with the condition $T_1 = 1 - X^2$ at $z = 1$, which satisfies (3.19*c*), and then we solve the steady-state forms of (3.11*a*) and (3.13) with the rest of (3.14), (3.15) and (3.19). This steady-state solution is used as the initial condition for each time integration.

We discretize the system of equations in space by using the Chebyshev spectral collocation method. We solve for the time-dependent unknown coefficients in the double Chebyshev polynomial series in X and z, and we evaluate (3.11*a*) and (3.13) at the Gauss–Lobotto collocation points. We use $NX + 1$ collocation points in the X-direction and $NZ + 1$ collocation points in the z-direction. Grid-independent solutions are achieved with $NX = 8$ for $\lambda \leqslant 8$ or $NX = 12$ for $8 < \lambda \leqslant 500$, and with $NZ = 8$ for $\lambda \leqslant 8$, $NZ = 14$ for $8 < \lambda \leqslant 100$, $NZ = 16$ for $100 < \lambda \leqslant 300$, $NZ = 18$ for $300 < \lambda \leqslant 400$, or $NZ = 22$ for $400 < \lambda \leqslant 500$. The total number of unknown functions of time is $NT = (NX + 1) \times (3NZ + 7)$ or 279 and 949 unknown functions for the smallest and largest values of λ considered here.

The time-dependent coefficients are integrated forward in time by the second-order-accurate Crank–Nicholson scheme. We found that an incremental time-step size of 0.01 gave time-step-independent results over the range of λ considered.

Since $R = Pr^{-1}M$, (3.11*a*) and (3.13) indicate that for a fixed value of Pr, the independent parameters are λ, M and k_y. We consider a response function of the system $G(\lambda; M, k_y)$ as the difference in T_1 at $X = 0$, $z = 1$ between two successive maxima, i.e. separated by one complete period in time of the oscillation. We construct

G from a time range that is much later than the initial transient of the system. For each value of λ, we systematically search the M, k_y space until we find the critical point when $G(\lambda; k_{yc}, M_c) = 0$ and $\partial G/\partial k_y(\lambda; k_{yc}, M_c) = 0$, where k_{yc} and M_c are the wave and Marangoni numbers for the critical mode, respectively. The first condition, $G = 0$, guarantees neutral stability, while the second condition, $\partial G/\partial k_y = 0$, guarantees the minimum M along the $G = 0$ locus for a given value of λ.

The numerical technique we used to solve this problem is now described by considering the contours of G in the (M, k_y)-plane. We fix the value of λ and find three points along the $G = 0$ locus by using a secant method (line search). For each of the three line searches, k_y is fixed and an M is found which gives $|G| < \delta$, where δ is our small convergence parameter. A parabola is then fitted to these three points and has the functional form of $M(k_y)$. We calculate the minimum point of the parabola and check to see if $|G| < \delta$ and $|\partial G/\partial k_y| < \delta$ at this point. If these conditions are not met then another line search is performed for the fixed k_y of the new point. With four points now identified on the $G = 0$ locus, one of the first three points is discarded by selecting the neighbouring points of the newest point. We construct another parabola, find the minimum of the parabola, and check for convergence again, etc. Typically 10 parabolic searches are required along with 7–10 function evaluations per line search in order to satisfy a convergence parameter of $\delta = 10^{-4}$, which is the limit of accuracy of the time-integration scheme for a time increment of 0.01. The total number of function evaluations (time integrations) is approximately, neglecting initialization and convergence checks, the product of the number of function evaluations for the line search and the number of parabolic searches, i.e. 70–100 function evaluations are required for each value of λ.

Our time-integration scheme represents an unusual way to find the critical normal mode. In a normal-mode analysis, ϕ_1, F_1, and T_1 would be replaced by the form

$$\phi_1(X, z, t) = \mathrm{Re}[\Phi(X, z) \exp(-\mathrm{i}\alpha t)], \tag{4.1}$$

where $\Phi = \Phi_r + \mathrm{i}\Phi_i$ is the complex modal function and α has the same meaning as the α in (1.7). For $L = O(\infty)$, the governing equations reduce to ordinary differential equations in z, but for $L = O(Ha)$, they reduce to partial differential equations in X and z. The Chebyshev polynomials and Gauss–Lobatto collocation points in X and z for a normal-mode analysis would be the same as those in our scheme. The normal-mode analysis would reduce to an eigenvalue problem involving square matrices with the dimensions $NT \times NT$. Of the NT eigenvalues α, we are only interested in the pair whose imaginary part first becomes non-negative as M is increased for each value of k_y. In our time-integration scheme, we choose an initial perturbation which includes all the normal modes, and then we integrate in time until all the modes with negative values of α_i decay, leaving only the critical normal mode. The basic algorithm for the normal-mode analysis is to find the NT complex eigenvalues, while that for our scheme is to perform a time integration for a sufficiently long period that all the modes have decayed except the critical one. For $L = \infty$, the normal-mode analysis is obviously better, because the number of collocation points for the ordinary differential equations is small and the number of eigenvalues is small. For any two-dimensional modal functions for a finite geometry, the matrices are much larger, so that the difference between the computational resources needed for the two approaches is smaller. We do not claim that our approach is better than a normal-mode analysis, but we do claim that it is equivalent. We chose this unusual approach because it provides the framework for future direct numerical simulations of the full nonlinear equations. We are only interested in one mode, namely the first mode to

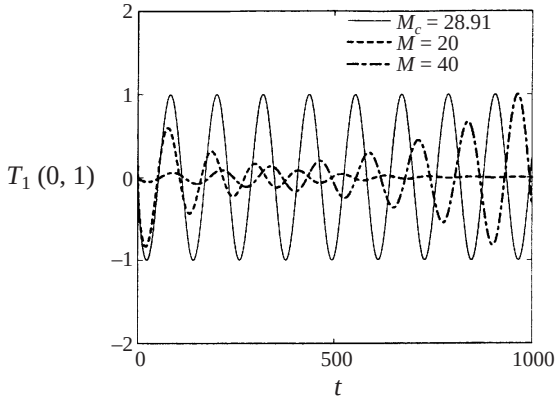

FIGURE 4. Typical oscillatory response in time of the perturbation temperature T_1 at the centre of the free surface $X = 0$ and $z = 1$. $\lambda = 0$, $Pr = 0.1$, $k = 0.627$, $M = 20$ (exponential decay), $M_c = 28.91$, and $M = 40$ (exponential growth).

begin to grow exponentially as the Marangoni number is increased past its critical value M_c. For $M > M_c$, several modes may be growing, and all growing modes are easily identified in a normal-mode analysis, while a filter would be needed to sort multiple modes in the present time-integration method. However, this paper does not treat the supercritical behaviour for $M > M_c$.

In figure 4 we show a typical time-history response of the perturbation temperature at the free surface taken at a point midway between the endwalls. The conditions are $\lambda = 0$, $Pr = 0.1$, $k = 0.627$, yielding a neutrally-stable response to the system for $M_c = 28.91$, and an exponentially decaying and growing response for $M = 20$ and $M = 40$, respectively.

5. Results

In figure 5(a) we show the critical Marangoni number M_c as a function of λ for the Prandtl number of molten silicon $Pr = 0.0269$ and for $Pr = 0.1$. For points along either line, a small disturbance leads to a neutrally-stable three-dimensional perturbation of the steady two-dimensional base flow, while above and below either line, small disturbances grow and decay exponentially in time, respectively. For $\lambda \geqslant 40$, the curves are linear and are given by $M_c = 7.1\lambda$ and $M_c = 11.8\lambda$ for $Pr = 0.0269$ and $Pr = 0.1$, respectively, while for $\lambda < 40$, there is a nonlinear region which approaches $M_c = 11.67$ and $M_c = 28.91$ as $\lambda \to 0$ for $Pr = 0.0269$ and $Pr = 0.1$, respectively. When $\lambda \to 0$, our results should match those of S & D. Since it is difficult to obtain precise values from the stability curve in figure 17 of S & D, we reproduced their analytic eigenvalue analysis with $k_x = 0$. We found that their value of $M_c^{S\&D} = 28.95$ for $Pr = 0.1$, which is within 0.14% of our result as $\lambda \to 0$. This agreement is indicated in the zoomed portion of figure 5a as the solid square on the M_c-axis which overlays our result. Since their solution for $L = \infty$ is analytic and essentially exact, while our numerical solution involves truncation errors in the spatial discretization and time integration, this comparison provides an estimate of the error in our numerical solution. The linear region of the curve represents a magnetically dominated flow which is confined to a free-surface layer with an $O(\lambda^{-1/2})$ thickness. We also show the critical Marangoni number vs. Pr for a fixed value of $\lambda = 100$ in figure 5(b). At $\lambda = 100$ the flow is magnetically dominated. Since $R = M/Pr$, the critical Reynolds

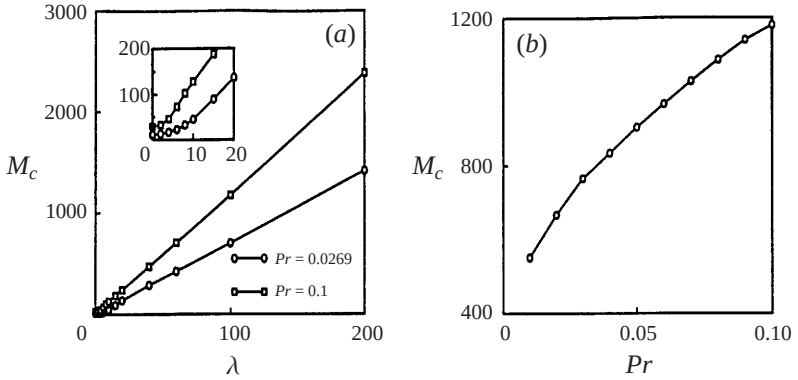

FIGURE 5. Critical Marangoni number (*a*) M_c vs. λ for $Pr = 0.0269$ and 0.1 and (*b*) M_c vs. Pr for $\lambda = 100$.

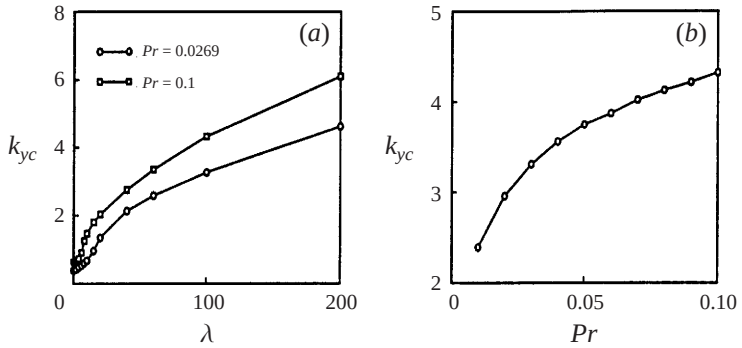

FIGURE 6. Critical wavenumber (*a*) k_{yc} vs. λ for $Pr = 0.0269$ and 0.1 and (*b*) k_{yc} vs. Pr for $\lambda = 100$.

number R_c increases as the value of Pr is decreased from 0.1 to 0.01. With all physical properties fixed except the thermal conductivity k, Pr decreases as k is increased, while R is independent of k and proportional to the basic temperature gradient b. As k is increased, thermal conduction carries more heat away from a hot spot or to a cold spot, so that a stronger convective heat transfer, reflected in a larger value of R_c, is needed to produce the instability.

The values of the critical-mode wavenumber k_{yc} are plotted as a function of λ in figure 6*a*. For $\lambda \geqslant 40$, there is a parabolic variation of k_{yc} with $k_{yc} = 0.33\lambda^{1/2}$ or $k_{yc} = 0.43\lambda^{1/2}$ for $Pr = 0.0269$ and $Pr = 0.1$, respectively. As $\lambda \to 0$ for $Pr = 0.1$, we find $k_{yc} = 0.627$, while $k_{yc}^{S\&D} = 0.628$, corresponding to a 0.16% error. We plot the S & D result in figure 6(*a*) as the solid square at $\lambda = 0$. In figure 6(*b*), k_{yc} is shown to increase monotonically with Pr for a fixed value of $\lambda = 100$. S & D found that the critical disturbance has the form of hydrothermal rolls propagating in a direction which is nearly orthogonal to the (X, z)-plane for fluids with $Pr \leqslant 0.1$. The length in the y-direction of each hydrothermal roll is given by π/k_{yc}, or 5.00 for S & D. When magnetic damping is introduced, the y-length of the rolls decreases, i.e. k_{yc} increases with increasing λ. As noted previously, $\partial u'/\partial x$ is negligible in (3.1*d*), while (3.10*b*,*c*) show that ϕ_1 is a stream function for w_1 and v_1 in each $X =$ constant plane. Therefore the contours of $\phi_1 \sin(k_y y)$ in any $X =$ constant plane are the streamlines for v_1 and w_1 in the hydrothermal waves. The contours in the $X = 0$ plane and at the time when v_1 is maximum are plotted in figure 7 for $\lambda = 6$ and $\lambda = 200$. Any axial variation of

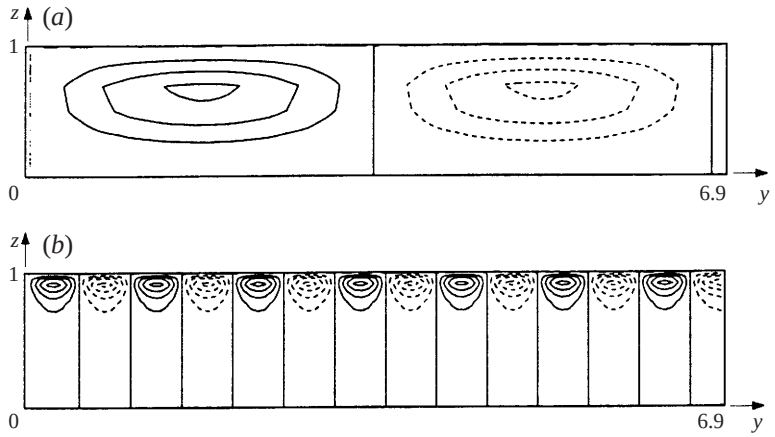

FIGURE 7. Contours of $\phi_1 \sin(k_y y)$ at $X = 0$ for the time when v_1 at $z = 1$ is maximum and for $Pr = 0.1$. Solid lines are positive contours and dashed lines are negative contours. (*a*) $\lambda = 6$ and (*b*) $\lambda = 200$.

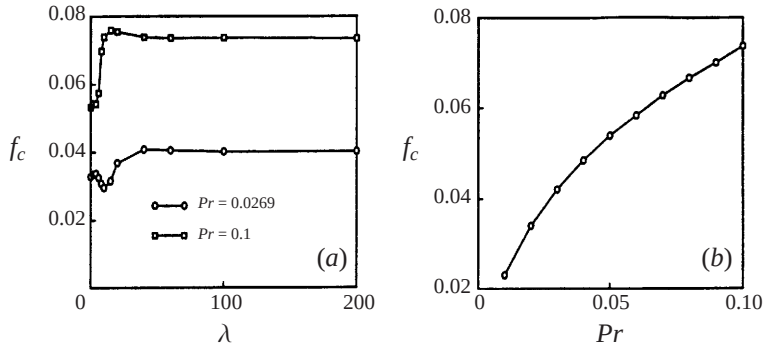

FIGURE 8. Critical non-dimensional circular frequency (*a*) f_c vs. λ for $Pr = 0.0269$ and 0.1 and (*b*) f_c vs. Pr for $\lambda = 100$.

ϕ_1 represents a change in the perturbation circulation in each $x =$ constant plane, but this variation is $O(Ha^{-1})$ except inside the Hartmann layers at $x = \pm L$. The contours in figure 7(*a*) for $Pr = 0.1$ show that the y-length of each hydrothermal roll shrinks from 5.00 to 3.45 as λ is increased from 0 to 6, but that the roll still extends through the full depth of the layer, as does the base flow in figure 2(*a*). The contours in figure 7(*b*) for $\lambda = 200$ show that the hydrothermal waves are now confined to a free-surface layer with an $O(\lambda^{-1/2})$ thickness, just like the base flow in figure 3*b*. For $\lambda = 200$, $k_{yc} = 6.08$, so that the y-extent of each roll has shrunk to 0.517. We estimate the z-extent of the hydrothermal waves for $\lambda \geqslant 40$ to be $3.0\lambda^{-1/2}$, so that the aspect ratio $(\Delta y/\Delta z)$ of each roll is $(\pi/k_{yc})/(3.0\lambda^{-1/2}) = 2.4$ for $\lambda \geqslant 40$. For $\lambda < 40$, the bottom blocks vertical motion, so that the aspect ratio is 5.0 for $\lambda = 0$ and 3.5 for $\lambda = 6$. Once the base flow and hydrothermal waves cease to be affected by the bottom wall, the aspect ratio is 2.4 with both Δy and Δz decreasing as $\lambda^{-1/2}$ with increasing λ.

In figure 8(*a*) the dimensionless circular frequency f_c of the critical mode is plotted as a function of λ. At $\lambda = 0$ and $Pr = 0.1$, $f_c = 0.053$, which matches the value we found from the analytical solution of S & D as indicated by the solid square at $\lambda = 0$ in figure 8(*a*). As λ increases for $Pr = 0.1$, f_c increases to a peak at $\lambda = 15$ and

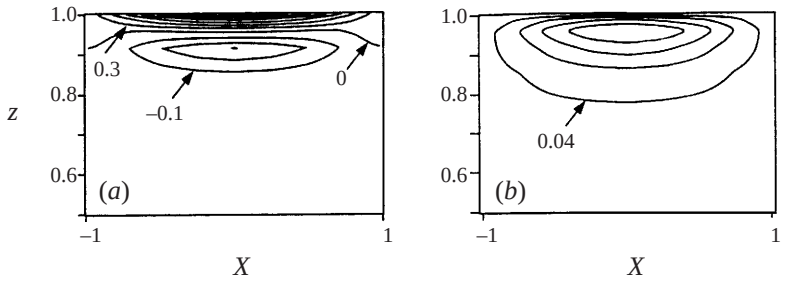

FIGURE 9. Contours of the perturbation velocities for $Pr = 0.1$ and $\lambda = 200$ at the time when v_1 at $X = 0$ and $z = 1$ is maximum. (*a*) $v_1 = -0.1i$ for $i = 0$ to 3, and $v_1 = 0.3i$ for $i = 1$ to 7. (*b*) $w_1 = k_y\phi_1 = 0.04i$ for $i = 1$ to 4. Hartmann layers match non-zero values of v_1 and w_1 at $X = \pm 1$.

then decreases to a constant value of $f_c = 0.073$ for $\lambda \geqslant 40$. As λ is increased, our core for $0 \leqslant z \leqslant 1$ splits into a central inviscid region near $z = 0.5$ and two parallel layers with $O(\lambda^{-1/2})$ thickness at $z = 0$ and $z = 1$. The two parallel layers just meet at $z = 0.5$ for $\lambda = 15$. The interesting peak at $\lambda = 15$ for $Pr = 0.1$ corresponds to the point when the two parallel layers begin to separate to leave an inviscid region near $z = 0.5$. Once λ reaches 40, the perturbations in the central inviscid region and bottom parallel layer have vanished, leaving only the perturbation in the top parallel layer. A similar trend occurs for $Pr = 0.0269$, but for a larger value of λ. Figure 8(*b*) indicates that the critical dimensionless circular frequency increases monotonically with Pr.

In order to illustrate the axial variations in the hydrothermal waves, we plot contours of $v_1(X, z, t_v)$ and $w_1(X, z, t_v)$ in figure 9, and the contours of $T_1(X, z, t_T)$ in figure 10 for $Pr = 0.1$, where v_1 or T_1 at $X = 0$ and $z = 1$ is maximum at $t = t_v$ or $t = t_T < t_v$, respectively. The velocities in figure 9 may be interpreted as a thermocapillary flow driven by the thermal field in figure 10, with a phase-lag of v_1 and w_1 behind T_1 due to inertial effects. At $t = t_T$ and $z = 1$, $T_1 \cos(k_y y)$ is positive and negative at $y = 0$ and $y = \pi/k_y$, respectively, so that flow is driven along the free surface from the hot line at $y = 0$ to the cold line at $y = \pi/k_y$, producing the positive values of v_1 in figure 9(*a*) at $y = \pi/2k_y$. The negative values of v_1 in figure 9(*a*) represent the return flow further from the free surface. The flow circuit is completed by upward flow, which is represented by the positive values of w_1 in figure 9(*b*) at $y = 0$ and which carries the cold fluid in figure 2(*b*) to the free surface, and by an equal downward flow near $y = \pi/k_y$. Clearly at $\lambda = 200$, the symmetry of the velocity contours indicates that the hydrothermal rolls travel in a direction orthogonal to the base state, i.e. corresponding to $k_x = 0$ for $L = \infty$.

The increase in M_c with increasing λ arises from the very small electric currents which fringe from the Hartmann layers for long distances into the core. The hydrothermal waves of S & D for $k_x = 0$ involve axial vorticity

$$\omega_x = \frac{\partial w}{\partial y} - \frac{\partial v}{\partial z} = \nabla^2 \phi. \tag{5.1}$$

Equation (3.11*a*) indicates that the important terms in (3.3) are

$$R\frac{\partial \omega_x}{\partial t} = \nabla^2 \omega_x + Ha^2 \frac{\partial j_x}{\partial x}, \tag{5.2}$$

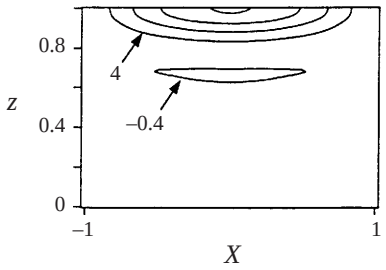

FIGURE 10. Contours of T_1 for $\lambda = 200$ and $Pr = 0.1$ and at the time when T_1 at $X = 0$ and $z = 1$ is maximum: $T_1 = 4i$ for $i = 1$ to 4 and $T_1 = -0.4$.

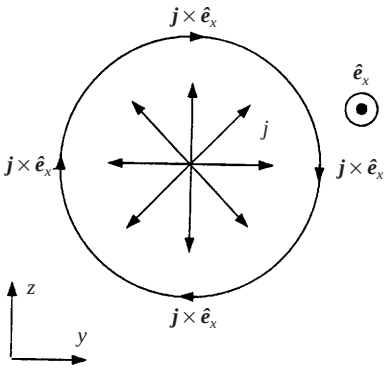

FIGURE 11. Sketch of net radially outward electric current from an axial line along which axial vorticity ω_x is positive. The circulation is counterclockwise while the EM body force is clockwise.

while the Hartmann conditions (3.18*b*) are

$$j_x = \mp Ha^{-1}\omega_x, \quad \text{at} \quad x = \pm L. \tag{5.3}$$

Figure 9 shows that ω_x is an even function of x. If $\omega_x > 0$ along some axial line through some point in the (y,z)-plane, then j_x is negative at $x = L$ and positive at $x = -L$, so that $\partial j_x/\partial x$ is negative along this axial line. Equation (5.2) indicates that electromagnetic effects accelerate the local decay of ω_x. Since $\partial j_x/\partial x < 0$ along this axial line, (3.1*e*) implies a net radially outward current from this axial line, as illustrated in figure 11. The net radially outward electric current interacts with the axial magnetic field $\hat{\boldsymbol{e}}_x$ to produce a clockwise EM body force opposing the counterclockwise circulation in figure 11 for $\omega_x > 0$. If $\omega_x > 0$ for $0 \leqslant y \leqslant \pi/k_y$, then $\omega_x < 0$ for $\pi/k_y \leqslant y \leqslant 2\pi/k_y$, so that electric current leaves both Hartmann layers for $0 \leqslant y \leqslant \pi/k_y$, fringes through the core and returns to the Hartmann layers for $\pi/k_y \leqslant y \leqslant 2\pi/k_y$. Since $\partial j_x/\partial x > 0$ for $\pi/k_y \leqslant y \leqslant 2\pi/k_y$, the net radially inward electric currents here provide an EM body force opposing the local clockwise circulation. Equation (5.3) shows that the axial currents created by the Hartmann layers at $x = \pm L$ are $O(Ha^{-1})$. Since the circuit for these Hartmann-layer currents is spread over an entire $O(Ha)$ length of the layer, the associated j_y and j_z are $O(Ha^{-2})$. Since the EM body force in the dimensionless momentum equation is multiplied by Ha^2, the EM damping or Joulean dissipation augments and is comparable to the $O(1)$ viscous dissipation.

The coupling of the axial vorticity ω_x in the hydrothermal waves, the axial velocity perturbation u', and the temperature perturbation T' is qualitatively the same with

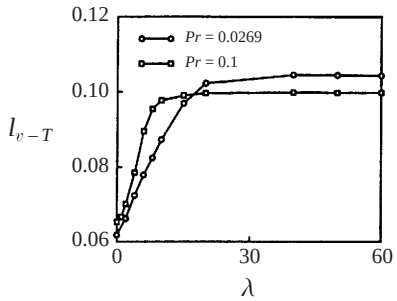

FIGURE 12. Normalized time lag l_{v-T} vs. λ for $Pr = 0.0269$ and $Pr = 0.1$.

or without magnetic damping, so that the discussion of S & D still applies here. Hot and cold free-surface perturbation temperatures at $y = 0$ and $y = \pi/k_y$ accelerate the local hydrothermal roll with $\omega_x > 0$. This roll convects cold and hot fluid to the hot and cold free-surface positions, respectively, so that the free-surface temperature perturbation is cancelled, but the hydrothermal roll continues because of inertia. The continuing roll involves convective heat transfer which creates cold and hot free-surface temperature perturbations at $y = 0$ and $y = \pi/k_y$ respectively. The temperature perturbation continues to increase until the associated surface-tension variation decelerates the hydrothermal roll to $\omega_x = 0$. The fluid is then stopped, but free-surface temperature perturbation remains and now accelerates a hydrothermal roll with $\omega_x < 0$ for the second half of each full period.

The lag l_{v-T} is the normalized time lag given as the time difference $t_v - t_t$ divided by the time for a period of an oscillation. We plot l_{v-T} vs. λ in figure 12. For $Pr = 0.1$, $l_{v-T} = 0.065$ at $\lambda = 0$ and increases to 0.099 for $\lambda \geqslant 20$. At $\lambda = 20$, the two $O(\lambda^{-1/2})$ thick parallel layers at $z = 1$ and $z = 0$ have separated, leaving an inviscid region in the centre of the fluid layer. For $\lambda = 0$, the time lag between the peak velocity and peak temperature is due to the flow overcoming the inertial effects as described by Smith (1986), while for $\lambda > 0$, the lag naturally increases since the flow must now overcome both the inertial effects and the magnetic body force.

Here and in S & D, the vertical velocity w_1 in the hydrothermal roll produces a perturbation of the axial velocity u_1 due to vertical convection of the base-flow velocity gradient, as reflected by $w_1 \partial u_c/\partial z$ in (3.9*a*). This u_1 is too small to play a significant role in the conservation of mass, i.e., in the circulation, but it does produce a significant convective heat transfer since the axial derivative of the base-flow temperature is -1, not $O(Ha^{-1})$, as reflected by the $-u_1$ term in (3.10*d*).

6. Conclusions

With a magnetic field parallel to the free surface of an electrically conducting fluid layer in a slot, the unsteady thermocapillary convection that develops from a steady, two-dimensional base state is damped by the magnetic body force. In the case of a slot with an infinite aspect ratio, the magnetic field has no effect on the two-dimensional base state and a very small effect on the three-dimensional perturbation of the base state. Significant effects of the magnetic damping first occur when the aspect ratio $2L$ of the slot is reduced from infinity to $O(Ha)$, where Ha is the large Hartmann number. We characterized this effect with the parameter $\lambda = Ha/L$, by plotting the critical Marangoni number, the wavenumber of the critical mode and the critical

frequency as functions of λ for $Pr = 0.026$ and $Pr = 0.1$. For large λ, the critical Marangoni number and critical wavenumber increase as λ and $\lambda^{1/2}$, respectively, while the critical frequency approaches a constant value. For large λ, both the base state and the disturbance of the base state were confined to a thin free surface layer with an $O(\lambda^{-1/2})$ thickness.

This work was supported by the National Aeronautics and Space Administration under Cooperative Research Agreement NCC8-90 and under a Graduate Research Fellowship and by the National Science Foundation under Grant CTS94-19484.

REFERENCES

Baumgartl, J., Gewald, M., Rupp, R., Stierlen, J. & Muller, G. 1990 The use of magnetic fields and microgravity in melt growth of semiconductors: a comparative study. *Proc. VIIth European Symp. on Materials and Fluid Sciences in Microgravity Oxford, UK, 10–15 September, 1989*, ESA SP-95. European Space Agency.

Braunsfurth, M. G. & Homsy, G. M. 1997 Combined thermocapillary-buoyancy convection in a cavity. Part II. An experimental study. *Phys. Fluids* **9**, 1277–1286.

Chandrasekhar, S. 1961 *Hydrodynamic and Hydromagnetic Stability*. Clarendon.

Croll, A., Dold, P. & Benz, K. W. 1994 Segregation in Si floating-zone crystals grown under microgravity and in a magnetic field. *J. Cryst. Growth* **137**, 95–101.

Davis, S. H. 1987 Thermocapillary instabilities. *Ann. Rev. Fluid Mech.* **19**, 403–435.

Gillon, P. & Homsy, G. M. 1996 Combined thermocapillary-buoyancy convection in a cavity: an experimental study. *Phys. Fluids* **8**, 2953–2963.

Hunt, J. C. R. 1965 Magnetohydrodynamic flow in rectangular ducts. *J. Fluid Mech.* **21**, 577–590.

Hurle, D. J. T. 1994 *Handbook of Crystal Growth, 2b: Bulk Crystal Growth*. Elsevier.

Kaddame, A. & Lebon, G. 1993 Overstability in Marangoni convection of an electrically conducting fluid in presence of an external magnetic field. *Microgravity Q.* **3**, 1–10.

Langlois, W. E. & Lee, K. J. 1983 Czochralski crystal growth in an axial magnetic field: effects of Joule heating. *J. Cryst. Growth* **62**, 481–486.

Maekawa, T. & Tanasawa, I. 1988 Effect of magnetic field on onset of Marangoni convection. *Intl J. Heat Mass Transfer* **31**, 285–293.

Mercier, J. F. & Normand, C. 1996 Buoyant-thermocapillary instabilities of differentially heated liquid layers. *Phys. Fluids* **8**, 1433–1445.

Morthland, T. E. & Walker, J. S. 1997 Convective heat transfer due to thermocapillary convection with a strong magnetic field parallel to the free surface. *Intl J. Heat Mass Transfer* **40**, 3283–3291.

Mundrane, M. & Zebib, A. 1993 Two- and three-dimensional buoyant thermocapillary convection. *Phys. Fluids* **5**, 810–818.

Pearson, J. R. A. 1958 On convection cells induced by surface tension. *J. Fluid Mech.* **4**, 489–500.

Priede, J. & Gerbeth, G. 1995 Hydrothermal wave instability of thermocapillary driven convection in a plane layer subjected to a uniform magnetic field. *Adv. Space Res.* **16**, 55–58.

Priede, J. & Gerbeth, G. 1997 Hydrothermal wave instability of thermocapillary-driven convection in a coplanar magnetic field. *J. Fluid Mech.* **347**, 141–169.

Riley, R. J. & Neitzel, G. P. 1998 Instability of thermocapillary-buoyancy convection in shallow layers. Part 1. Characterization of steady and oscillatory instabilities. *J. Fluid Mech.* **359**, 143–164.

Robertson, G. D. & O'Connor, D. 1986 Magnetic field effects in floating-zone Si crystal growth. III. Strong axial magnetic fields. *J. Cryst. Growth* **76**, 111–122.

Rupp, R., Auerochs, S., Muller, G., Weyrich, C. & Leibenzeder, S. 1991 Growth of GaAs single crystals by the floating zone technique under microgravity. *Adv. Space Res* **11**(7), 297–304.

Saedeleer, C., De Garcimartin, A., Chavepeyer, G. & Platten, J. K. 1996 The instability of liquid layer heated from the side when the upper surface is open to air *Phys. Fluids* **8**, 670–676.

Sen, A. K. & Davis, S. H. 1982 Steady thermocapillary flows in two-dimensional slots. *J. Fluid Mech.* **121**, 163–186.

Series, R. W. & Hurle, D. T. J. 1991 The use of magnetic fields in semiconductor crystal growth. *J. Cryst. Growth* **113**, 305–328.

Shen, Y., Neitzel, G. P., Jankowski, D. F. & Mittelmann, H. D. 1990 Energy stability of thermocapillary convection in a model of the float-zone crystal-growth process. *J. Fluid Mech.* **217**, 639–660.

Smith, M. K. 1986 Instability mechanisms in dynamic thermocapillary liquid layers. *Phys. Fluids* **29**, 3182–3186.

Smith, M. K. & Davis, S. H. 1983 Instabilities of dynamic thermocapillary liquid layers. Part 1. Convective instabilities. *J. Fluid Mech.* **132**, 119–144 (referred to herein as S & D).

Thess, A. & Nitschke, K. 1995 On Benard-Marangoni instability in the presence of a magnetic field. *Phys. Fluids* **7**, 1176–1178.

Velten, R., Schwabe, D. & Scharmann, A. 1991 The periodic instability of thermocapillary convection in cylindrical liquid bridges. *Phys. Fluids* **3**, 267–279.

Walker, J. S., Ludford, G. S. S. & Hunt, J. C. R. 1972 Three-dimensional MHD duct flows with strong transverse magnetic fields. Part 3. variable-area rectangular ducts with insulating walls. *J. Fluid Mech.* **56**, 121–141.

Wilson, S. K. 1993 The effect of a uniform magnetic field on the onset of Marangoni convection in a layer of conducting fluid. *Q. J. Mech. Appl. Maths* **46**, 211–248.

Wilson, S. K. 1994 The effect of a uniform magnetic field on the onset of steady Marangoni convection in a layer of conducting fluid with a prescribed heat flux at its lower boundary. *Phys. Fluids* **6**, 3591–3600.

Zebib, A. 1996 Thermocapillary instabilities with system rotation. *Phys. Fluids* **8**, 3209–3211.